



A sensor enabled robotic strategy for automated Defect-Free Multi-Pass High-Integrity welding

Names: Charalampos Loukas^{a,*}, Veronica Warner^b, Richard Jones^b, Charles N. MacLeod^a, Momchil Vasilev^a, Ehsan Mohseni^a, Gordon Dobie^a, Jim Sibson^b, Stephen G. Pierce^a, Anthony Gachagan^a

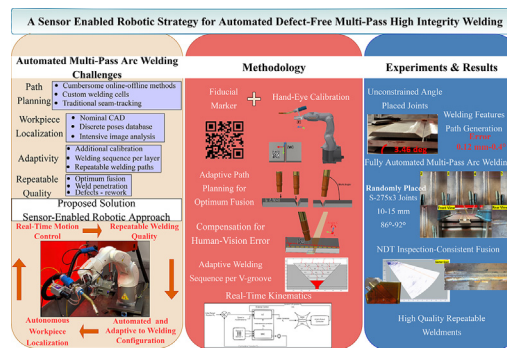
^a Sensor Enabled Automation Robotics & Control Hub (SEARCH), Department of Electronic & Electrical Engineering, University of Strathclyde, Glasgow G1 1XQ, UK

^b Babcock International Group PLC, Devonport Royal Dockyard, Plymouth, Devon, PL1 4SG

HIGHLIGHTS

- An adaptive robotic welding approach is presented for fully automated defect free multi-pass robotic arc welding.
- A user-initiated, workpiece localization method without any prior component knowledge is introduced utilizing Hand-Eye calibration.
- An algorithmic process compensates for human-vision error by adapting the welding process to the pre-welded specimen for on-the-fly welding path generation.
- Robotically experimental verification on welded joints of single sided butt joints is demonstrated.
- Non-Destructive Testing in the form of Ultrasound Testing validates the high integrity and repeatable quality of the proposed work.

GRAPHICAL ABSTRACT



ARTICLE INFO

Article history:

Received 26 August 2022

Revised 14 November 2022

Accepted 22 November 2022

Available online 24 November 2022

Keywords:

Robotic Arc Welding

Path Planning

Defects

Multi-Pass

V-groove

Non-Destructive Testing

ABSTRACT

High-integrity welds found in safety-critical industries require flaw-free joints, but automation is challenging due to low-volume, often-unique nature of the work, alongside high-uncertainty part-localisation. As such, robotic welding still requires tedious manually taught paths or offline approaches based on nominal Computer-Aided-Design (CAD). Optical and laser sensors are commonly deployed to provide online adjustment of pre-defined paths within controlled environments. This paper presents a sensor-driven approach for defect-free welding, based on the as-built joint geometry alongside the requirement for no-accurate part localisation or CAD knowledge. The approach a) autonomously localises the specimen in the scene without CAD requirement, b) adapts and generates accurate welding paths unique to the as-built workpiece and c) generates robot kinematics based on an external-control strategy. The proposed approach is validated through experiments of unconstrained placed joints, where the increased accuracy of the generated welding paths, with no common seam tracking, is validated with an average error of 0.12 mm, 0.4°. Coupling with a multi-pass welding framework, the deployment of fully automated robotic arc welding takes place for different configurations. Non-Destructive-Testing

* Corresponding author.

E-mail address: charalampos.loukas@strath.ac.uk (Names: Charalampos Loukas).

(NDT) in the form of Ultrasound-Testing (UT) inspection validates the repeatable and flaw-free nature of the sensory-driven approach, exploiting direct benefits in quality alongside reduced re-work.

© 2022 The Author(s). Published by Elsevier Ltd. This is an open access article under the CC BY-NC-ND license (<http://creativecommons.org/licenses/by-nc-nd/4.0/>).

1. Introduction

Staying productive and competitive in global High-Value Manufacturing (HVM) sectors as product complexity and volumes rise remains a significant challenge. Despite the significant integration of robotic welding in HVM sectors, these systems are often only viable and programmed to perform repetitive, part and location constrained, high-volume tasks in application specific welding cells [1]. When considering high-integrity welds, as those found in safety-critical industries such as nuclear, defence and oil & gas, the requirement for defect, or flaw-free joints is critical alongside the challenge of often-unique fabrications [2]. Presence of common welding defects such as porosity or lack of fusion only detected at full-volume completion can add further delays to the overall manufacturing process by requiring rework or even leading to scrapping when failing to pass acceptance standards [3,4]. Automation of such welds which often feature thick sections and multi-pass welds across layers, still suffer from tedious robotic path planning approaches and lack of adaption of the welding process to different configurations. Furthermore, due to the low-volume nature of such fabrications the opportunity for highly controlled and accurate part fixturing and localisation is often deemed commercially unviable due to cost. The ratio of set-up time of weldments in controlled fixtures over production can account for more than 95 % [5] and therefore reducing time associated with any fixturing is desired. Additionally, when considering repair of high-integrity welds of ageing assets, further welded groove positional uncertainty exists due to inconsistencies between drawings and in-service variations.

While an increasing number of automated robotic welding systems commonly feature laser profilers, these are often only utilised to adapt pre-programmed paths originating from CAD of the workpiece, as part of constrained repetitive tasks. When the specimen's position and orientation changes or the geometric characteristics of the groove vary relative to the nominal then additional cumbersome time is required to adjust a) the robotic programming to generate new welding paths and subsequently b) the welding schedule of passes and welding parameters per layer. In addition, high tolerance requirements must be ensured and misalignments during fabrication fitting and gap width variation must be addressed in combination with an adaptive strategy to ensure high quality repeatable welds. These requirements and current limitations, drive the need for an intelligent and sensor-enabled automated welding solution, as presented herein, capable of dynamic generation and optimisation of the process to ultimately deliver flaw-free welds.

1.1. Automated robotic welding

When considering automated welding, articulated robotic welding systems commonly featuring six Degrees of Freedom (DoF), are deployed due to their flexibility in motion and high repeatability. These systems can support a wide range of different arc welding processes, such as Gas Metal Arc Welding (GMAW), Tungsten Inert Gas (TIG), Submerged Arc Welding (SAW) [6].

The two main categories of robot path planning are Online Programming (OP) and Offline Programming (OLP) methods, where also Visual Servoing (VS) control schemes and sensory-guided methods aim to deliver automated path planning strategies [7–

12]. OP requires operator's input to define the path points in space manually through the teach pendant. Hence, is characterized as a time-consuming method with drawbacks such as mandatory downtime between jobs. On the other hand, OLP relies on the existence of accurate CAD of the workpiece and a customized welding cell setup. This method is superior for large volume production but still, is characterized by tedious programming overhead to compensate for deviations between the design and the actual workpiece. Path planning generated from vS guides the robotic arm with respect to a target object based on nominal CAD and on vision feedback. vS approaches are characterized by high computation load and a requirement for nominal CAD to calculate inverse kinematics and deploy real-time image processing algorithms [13]. To overcome challenges related to unstructured environments the use of sensors such as optical and tactile, mainly to introduce feedback on the robot programming task, constitutes sensor-guided programming [9,14]. The main advantages of the sensor-guided approaches are the integration of motion programming within the production process and the consideration of the actual as-built workpiece rather than the CAD design [15].

1.2. Workpiece localization

The current prevalent method for workpiece localization in welding applications is feature matching [16–18], accomplished by the use of tactile, laser or 3D sensors, mounted on robot end-effector or in a static fixture within the welding cell to extract point cloud data of the workpiece [19]. Research projects, such as MARWIN aimed to provide automated welding capabilities for SMEs [20] and HEPHAESTOS I & II, a candidate for ship repair welding fabricated parts [21], were developed based on the use of CAD data to generate robot paths. Assuming an approximate pose of the workpiece, the extracted features are aligned with the reference CAD, usually with a local minimization algorithm, such as Iterative Closest Point (ICP) [5,22,23]. This approach is not efficient in terms of high product variance and small volume components. Global techniques are adopted such as clustering pose candidates [24,25] and voting schemes [26,27]. However, the accuracy of these methods depends on the existence of a database containing discrete reference poses of the workpieces which are not possible in an unstructured welding environment. As a result, in welding applications, a global localization approach is absent compared to other automated production systems, such as bin picking [19]. Table 1.1 depicts the current state-of-the-art regarding automated workpiece localization linked to automated path planning approaches along with their limitations.

1.3. Contribution to novelty

To automate multi-pass, high-integrity, defect-free welding in unstructured environments, it is crucial to a) autonomously and accurately generate the welding paths based on the actual as-built pre-welded joints, and not use nominal CAD, generated offline programming, b) adapt the pose of the welding torch relative to the specimen in a repeatable manner, based again on actual as-built pre-welded components to maximize fusion and c) adapt the welding sequence of welding parameters per welding layer based on the geometric characteristics of the groove as it is deposited, while conforming with pre-approved Welding Procedure Specifica-

Table 1.1
Relevant works in automated robotic workpiece localization.

| Relevant Works | No need for Nominal CAD | No need for an Initial pose guess | No need for a database of discrete poses | Not a Computative Intensive Image Analysis * | Verification of High-Integrity defect free welds |
|-----------------------------|-------------------------|-----------------------------------|--|--|--|
| Mitchell Dinham et al. [28] | ✓ | ✓ | ✓ | x | x |
| MARWIN [20] | x | ✓ | ✓ | x | x |
| HEPHAESTOS I & II [21] | ✓ | ✓ | ✓ | x | x |
| K.T. Gunnarsson [16] | x | ✓ | ✓ | ✓ | x |
| Xiong et al [17] | x | ✓ | ✓ | ✓ | x |
| M. Rajaraman et al. [5] | x | x | ✓ | ✓ | x |
| Cheng-Hei Wu et al. [24] | x | ✓ | x | ✓ | x |
| L.Yang et al.[29] | x | ✓ | ✓ | x | x |
| This body of work | ✓ | ✓ | ✓ | ✓ | ✓ |

*Intensive image analysis refers to image segmentation, applying window ROI, edge detection, 3D reconstruction.

tion (WPS) document. Here in this paper, a series of novel developments are presented towards full end-to-end automation of high-integrity, defect-free, multi-pass robotic arc welding within unstructured environments:

1. User-initiated, autonomous workpiece localization of the pre-welded joint based on a no *priori* CAD or component information, ensuring multiple welded joints in correct sequence.
2. Adaption of the welding torch's pose, and hence deposition, to the unknown, as-built, pre-welded joint configuration.
3. External real-time sensor-enabled robot kinematics for on-the-fly path-planning.
4. Incorporation of autonomous multi-pass welding deposition sequence, based on a cost function optimisation concept.

Considering each of these to automate welding in unstructured environments, there may be times where multiple un-welded joints are required to be fused within the working volume of the robot. The sequence in which these is undertaken is often critical from a geometrical, process and distortion perspective. This paper does not seek to address this significant challenge and hence uses a simpler solution of a user-initiated and deployed concept of common fiducial Quick Response (QR) codes which indicate joint 1, 2, 3 etc. and hence the welding sequence accordingly. The fine approximate localization of the specimen is then achieved through combination of the QR code tag and hand-eye calibration, avoiding the need for any manual, offline programming or a feature matching approach nominal based on the existence of a CAD. The key benefits of adapting the pose of the torch for a pre-welded joint, include i) maximum accessibility, ii) heat concentration and coverage for all three degrees of orientation in cartesian space as well as iii) the accurate extraction of geometry characteristics and key points of the weldment for on-the-fly welding path generation. Finally, the generation and deployment of kinematics through an external real-time position control strategy eliminates the need for any CAD based OLP programming, manual teaching of robotic paths or manual intervention during welding. As a result, these contributions raise the level of flexibility to weld different V-grooves in an unstructured environment, by minimizing human input and ensuring repeatable welding quality.

The rest of this paper is organised as follows: Section 2 introduces the methodology regarding the workpiece localization, the adaption of the pose of the torch and external control of kinematics. Section 3 demonstrates the experimental setup for various welding configurations of V-grooves, for automated localization, adaption to the welding configuration for accurate extraction of

features and generation of welding paths. To verify the high-integrity nature of the welds under the proposed strategy, Phased Array Ultrasonic Testing (PAUT) inspection is undertaken to inspect for any potential defects and verify the high-integrity output of the solution. The subsequent proof-of-concept demonstration results are discussed in Section 4 with Section 5 concluding this paper. In addition, in Appendix 6.1 a permanent link demonstrating the novel developments of the sensory-driven welding approach is included.

2. Methodology

2.1. Workpiece localization

For the successful localization and 3D pose estimation of the welding specimen its pose is required relative to the welding system. Hand-eye calibration can determine the 3D pose (orientation and translation) between the vision system and the end-effector [30]. For the extraction of features able to construct the 3D pose of the specimen, different global techniques have been investigated so far. Edge detection [28,31], image segmentation [28,32,33], the use of predefined Region of Interest (ROI) [34,35] and utilization of RGB-D sensors for point cloud extraction have been explored [36]. These methods are proved resilient in a controlled environment and not in a production floor which are usually affected by varying contrast, spatial distortion, varying lighting and fixtures in place requiring fine-tuning of pattern recognition algorithms to identify the welding component in different configurations [37]. Fig. 2.1 describes the hand-eye robotic welding system where the camera is mounted on the end-effector (eye on hand) along with the homogeneous transformation matrices.

The homogeneous equation $AX = XB$, where A describes the robot motion and B the camera induced motion can be used to solve the hand-eye transformation X [38,39]. The result of the calibration which is the gHe can be used to find the 3D pose of the weld specimen relative to the robot active motion frame as given by Eq:2:1:

$$bHw = bHg \cdot gHe \cdot eHw \quad (2.1)$$

In parallel, the calibration of the camera system to compensate for the lens, radial and tangential distortion, can be established from the collected frames [40]. The result is the intrinsic matrix K described by Eq:2:2 and the radial and tangential distortion coefficients k_1, k_2, k_3, p_2, p_3 which define the camera parameters, with (f_x, f_y) to be the focal point of the camera and (c_x, c_y) stands for

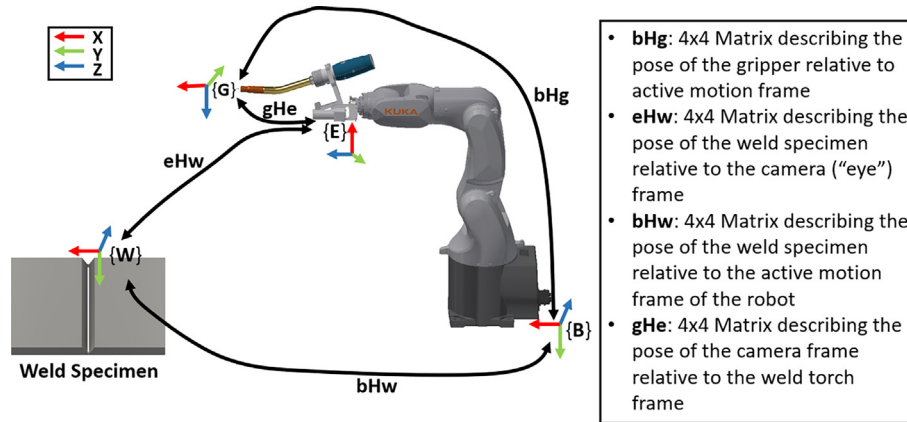


Fig. 2.1. Hand-Eye calibration and relative coordinate transformations. Letters B, E, G and W stands for robotic Base, Eye (camera) frame, Gripper and Weld specimen respectively.

the principal point. The bHg transformation is extracted from the robot controller and only eHw which is the extrinsics of the camera needs to be estimated. As a fiducial marker, a QR code is used (Fig. 2.2 (b)) which can provide distinguishable image features to estimate the eHw and has been proved a resilient and robust solution in a

$$\begin{bmatrix} f_x & 0 & c_x \\ 0 & f_y & c_y \\ 0 & 0 & 1 \end{bmatrix} \quad (2.2)$$

variety of robotic applications, such as object manipulation tasks and autonomous driving of mobile robots [41,42]. Within this work, the use of the QR code is utilized as a user-driven method to identify the position and the 3D pose of that welding joint in the scene among the existing, to be welded, sequencing in that way welding jobs to the robotic welding system. In that way the dependence on the actual characteristics of the workpiece is bypassed, usually affected by the background environment or existing fixtures and clamping.

The estimation of eHw which is the 3D pose of the QR code relative to the vision system can be solved using the Perspective-three-Point (P3P) algorithm [43]. Following that, to relate the 3D pose of the QR code with the 3D pose of the specimen, the following convention depicted in Fig. 2.2(a) is followed, where one side of the square fiducial marker is placed in parallel with the main axis of welding. For a QR code with edge size equals to m and identified corners in image plane $\{I\}$ of sequence $I_1-I_2-I_3-I_4$, the corresponding

world points $W_1-W_2-W_3-W_4$ which all lie in the specimen plane can be set according to Eq:2:3 to define the direction of the axes frame $\{W\}$ of the QR code, such as Y is the main axis of welding for the specimen.

$$\left. \begin{matrix} I_1 = (u_1, v_1) & W_1 = (0, 0, 0) \\ I_2 = (u_2, v_2) & W_2 = (0, m, 0) \\ I_3 = (u_3, v_3) & W_3 = (m, m, 0) \\ I_4 = (u_4, v_4) & W_4 = (m, 0, 0) \end{matrix} \right\} \quad (2.3)$$

2.1.1. Adapting to the welding configuration

Optimum heat concentration, weld pool penetration and sufficient fusion with the base plates are key aims when considering high-integrity welding. The positioning of the welding torch is described by the work and travel angles as shown in Fig. 2.3, where incorrect parameters can cause adverse effects such as porosity, weld undercut and slag entrapment [44].

2.1.2. TCP calibration and Initial pose adjustment

To adjust the work and travel angle requires extraction of the pose of the specimen and the motion of the Tool Centre Point (TCP) of the end-effector relative to the extracted pose. The calibration of the TCP beforehand aids the alignment of the welding torch relative to the specimen. As shown in Fig. 2.4 (b) the TCP is calibrated such as the X-axis is pointing in the direction of the electrode wire and the orientation of the Z-axis forms 90° with the electrode wire passing through the middle plane of the torch.

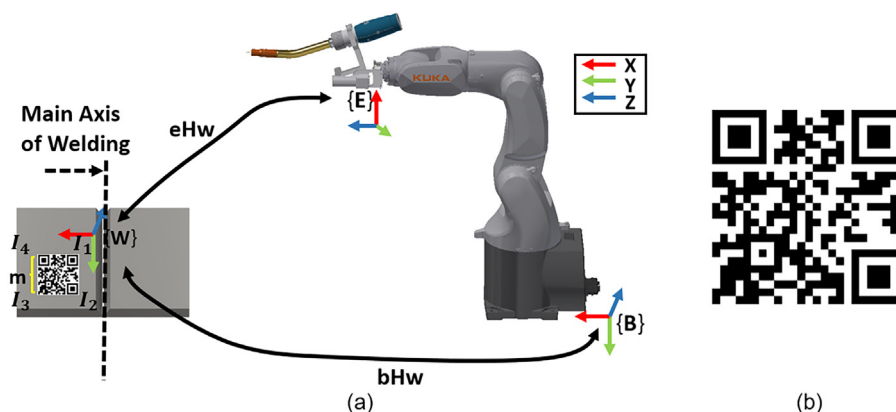


Fig. 2.2. (a) Fiducial QR code marker placed in the weld joint to reveal the pose of the welding specimen, (b) QR code used as fiducial marker.

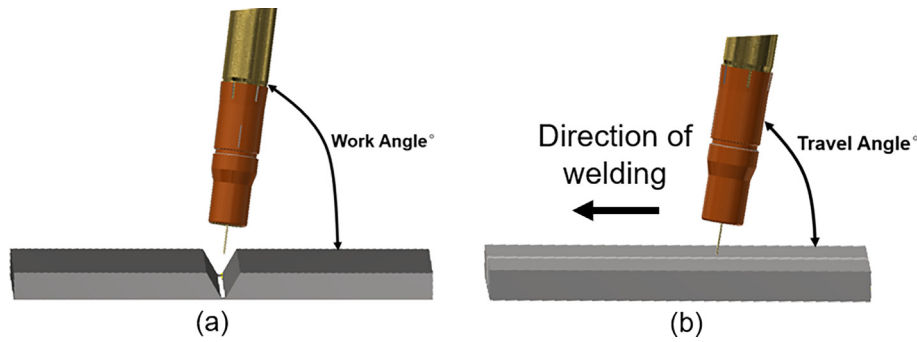


Fig. 2.3. Orientation of the torch during welding: (a) Indicates the work angle of torch formed by a line perpendicular to the major surface of the workpiece and a plane determined by electrode axis and weld axis (b) The travel angle of the torch dictates the welding technique which can be forehand or backhand, based on the direction of the electrode relative to the welding direction [44].

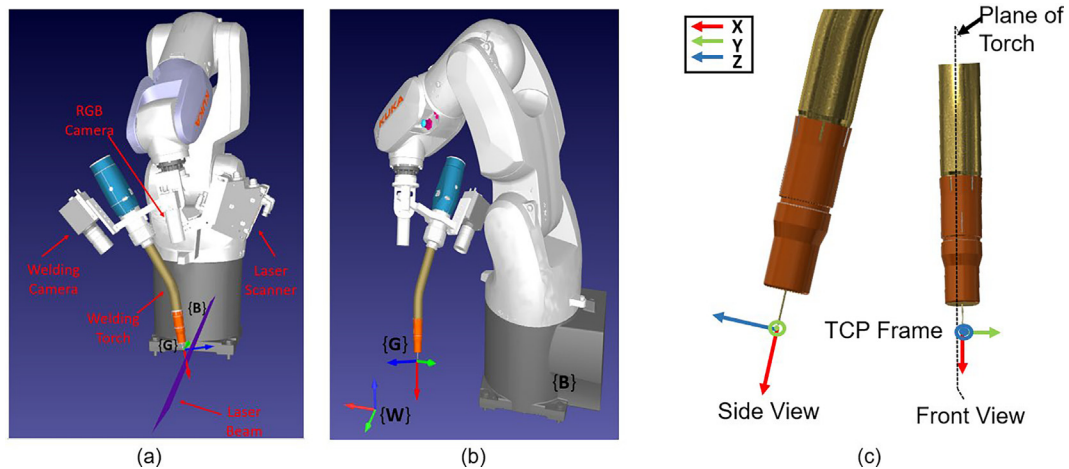


Fig. 2.4. (a) Robotic setup consists of a welding camera, RGB camera, welding torch and laser scanner, (b) Front-view showing the specimen's frame {W} relative to gripper {G}, (c) TCP calibration of the welding torch.

The adjustment of the pose of the torch {G} for a specimen with pose {W} relative to robot base {B} (Fig. 2.4 (b)), is described by the Euler angles A, B, C or angle psi, work angle and travel angle respectively. The first target, moving the TCP relative to frame {W}, is assigned Euler angles following the ZYX convention of KUKA, of $A = 90^\circ$, $B = 80^\circ$, $C = 0^\circ$. In that way, irrespective of the orientation of the specimen frame {W} relative to the robot base {B}, a 90° work angle is achieved, and a start travel angle of 10° which is used commonly in forehand welding. The angle C is selected to be 0° for the laser scanner which is mounted in the welding torch to align the projected laser stripe 90° relative to the main axis of welding Y, employing the full range of the scanner to extract features of the V-groove.

2.1.3. Compensating for vision and human error through optical sensing

Since a human place the fiducial marker, an error can be introduced in the pose of the QR code which represents the specimen's pose. Additionally, an error is accumulated from the TCP, camera, and hand-eye calibration, referred here from now on as vision error. Following the initial torch's pose adjustment, the TCP is assigned the second target relative to the frame of motion {W} to approach the origin of the QR code $X = 0$, $Y = 0$, $Z = 0$. A touch sensing routine is developed (Algorithm 1) and utilized to drive the welding torch within the V-groove.

The placement of the QR code as depicted in Fig. 2.5 (a) introduces an error in angle A which describes the orientation of the

specimen around axis Z of QR code frame {W}. To compensate for the error in angle A between the QR frame {W} and the actual orientation of the specimen, an inspection process takes place, where the TCP of the welding torch continues to move back at the start and end of the specimen relative to the identified frame {W} while the laser scanner identifies the middle of the seam to record P_{start} and P_{end} points along with their X and Y coordinates. In that way, the corrected slope of the seam path in the X-Y plane of {W} is calculated and the arctan of that slope is added as angle difference relative to the extracted angle A (Algorithm 2).

At the same time, an error can exist also in angle C which describes the orientation of the specimen around axis X of frame {W} and is linked to the travel angle. Due to this error the laser scanner (Fig. 2.6), which follows the induced motion of the welding torch will not move to a constant height relative to the specimen, providing false measurements in the set Region of Interest (ROI) regarding bevel height, root-face, and root gap measurement. To compensate, in the above inspection process, the TCP visits three key points moving relative to the motion frame {W} middle, start and end of the specimen. In each one, the distance of the laser scanner from the specimen must be equal to the predefined distance of the laser scanner from the top of the specimen, recorded in the middle key point.

The predefined distance is selected to be within the standard measuring range of the laser scanner according to manufacturer specifications to output reliable measurements. As the robotic arm progresses to the start and end of the specimen, the feedback

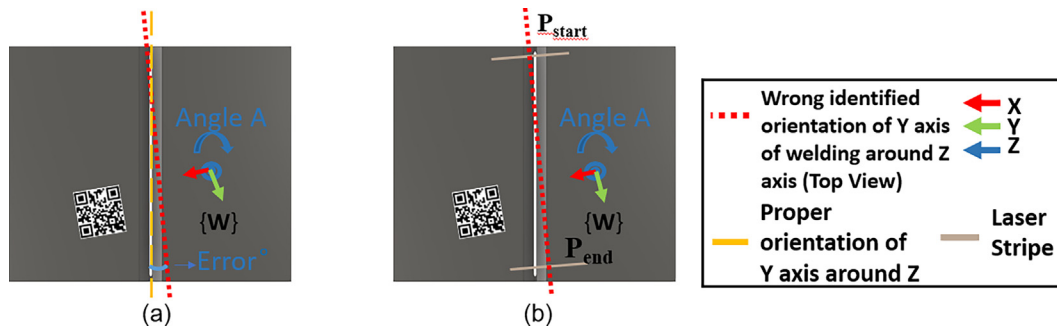


Fig. 2.5. Misplacement of QR code affect the angle A of torch relative to Z-axis of {W}: (a) The wrong axis of welding forms angle A + error° around the desired axis of welding, (b) P_{start} and P_{end} are recorded while the laser scanner moves the TCP to the middle of the seam and X, Y coordinates of the TCP are recorded on these points.

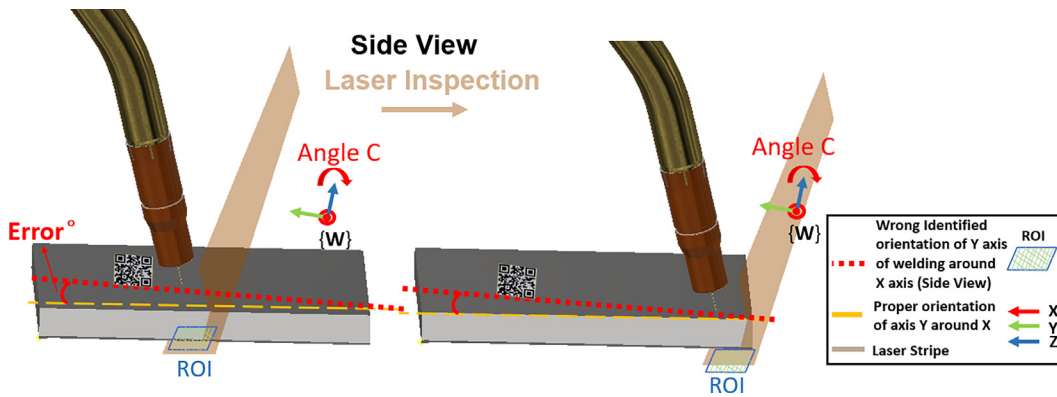


Fig. 2.6. Error in angle C causes the laser scanner to inspect in different heights over the specimen length, causing the ROI for gap measurement to offset from the desired area of inspection.

from the scanner offsets the TCP of the welding torch to match the predefined distance from the surface, recording the coordinates of Y_{start} , Z_{start} and Y_{end} , Z_{end} of the TCP in Y-Z space. These are used to calculate the slope of the seam path in Y-Z plane of {W}, and the arctan of this slope is added as the angle difference in the original measured angle C (Algorithm 3). Finally, the error in angle B which represents the orientation of the specimen around the Y-axis (the main axis of welding), is identified from the internal measurement of the laser scanner using the inherent principle of triangulation. The developed vision approach (hand-eye, laser sensing) with the above algorithmic process makes it feasible to generate welding paths on-the-fly for an unstructured environment and the unconstrained placement of specimen. At the same time, builds on practices from manual welding to maximize welding fusion, whereas automated welding systems feature the adjustment of pre-programmed welding paths through common seam tracking.

Following the compensation of the vision error, the extraction of the V-groove characteristics and the reference welding path takes place using the laser scanner. These processed features are used as inputs to the multi-pass welding framework to populate the welding schedule [45]. The TCP of the welding torch moves relative to the new corrected frame {W}, as depicted in the flowchart of Fig. 2.7. The described process identifies the start–end points when a step change in bevel height of more than 5 mm is identified marking the start–end of the specimen. The key features of the V-groove, root-face, root-gap, groove angle, length of specimen, bevel-height, are extracted utilizing the inherent functions of the laser scanner, two pre-defined reference lines separated in 100 mm distance and a set ROI anchored to follow the top of the specimen, able to enclose the root-face feature for thicknesses between 8 mm – 20 mm [46]. The 100 mm distance is sufficient

to identify and capture V-grooves, where the groove angle range between 60°–120°, commonly encountered in industrial configurations. The utilized robot speed for feature extraction and the sampling rate per distance of the specimen are selected to align with the number of profiles that the scanner is configured to avoid any under sampling. These values are shown in Section 3.1 along with the configuration of the laser scanner (Table 3.1). The processing algorithm of these features consists of outliers’ detection utilizing the upper and lower limit of the interquartile range technique for both directions of inspection and averaging of values along the welding specimen [47].

2.2. External control and real-time deployment of kinematics

The autonomous optical-tactile approach, the investigation of the optimum pose of the welding torch relative to the welding joint and the generation of robotic welding path is underpinned by an external real-time motion module. The developed method consists of a trajectory control algorithm and builds upon a Robotic Sensor Interface (RSI) protocol which allows TCP position adjustments based on a fixed interpolation timestamped cycle of 4 ms to purely control and generate robotic motion [48].

The developed control algorithm executes at the RSI interpolation cycle and is presented in the process diagram of

Fig. 2.8 [49]. It consists of a Linear Controller (LC) which is based on an acceleration - cruise trajectory profile with setpoint speed v , acceleration set by the user and generates the required linear increment component d_l between the current end-effector position P_c and target P_T for each axis. In addition, a Sensor Adaptive Input Controller (SAIC) serves the multiple sensors feedback, by translating and deriving the output to instantaneous correction

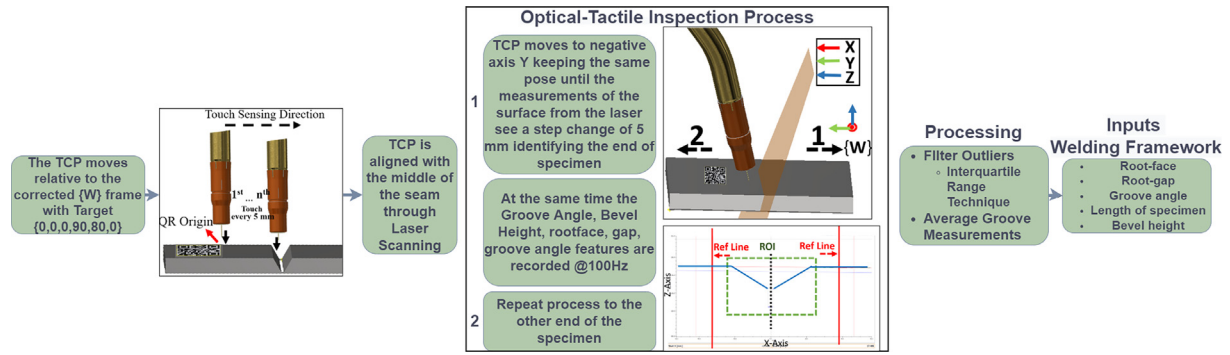


Fig. 2.7. The V-groove dynamic inspection process for generating the root-pass path used as a reference welding path and measurement of geometric characteristics are used as inputs for the multi-pass welding framework [43].

Table 3.1 Robotic and Welding Equipment Layout.

| # | Equipment | Laser Scanner Configuration |
|----|---|-----------------------------|
| 1 | KUKA KR3-R540 | Exposure-1.5 ms |
| 2 | Scan-Control 2910-100/BL | No. profiles-100 Hz |
| 3 | TBi Weld Torch 22° | Saturation-78 % |
| 4 | XIRIS XVC 1000 | Median Filter-5 Taps |
| 5 | Blackfly RGB PGE50S5C | Sampling Distance -1 mm |
| 6 | TBi Weld Torch Hose 1.2 m | Inspection Distance -140 mm |
| 7 | Jackle Robo Wire Feeder | |
| 8 | Jackle 400 V ProPulsWelder | |
| 9 | Gas ArCO ₂ (80 % Ar + 20 % CO ₂) | |
| 10 | 3x Magnets (40 kg Force) | |

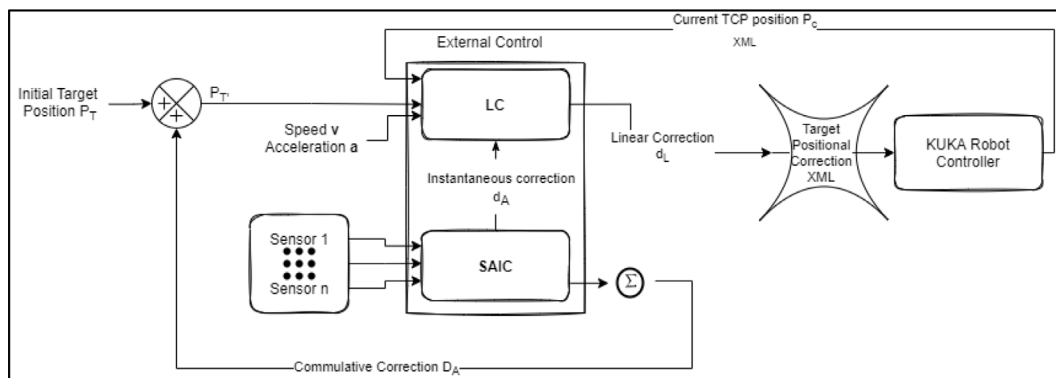
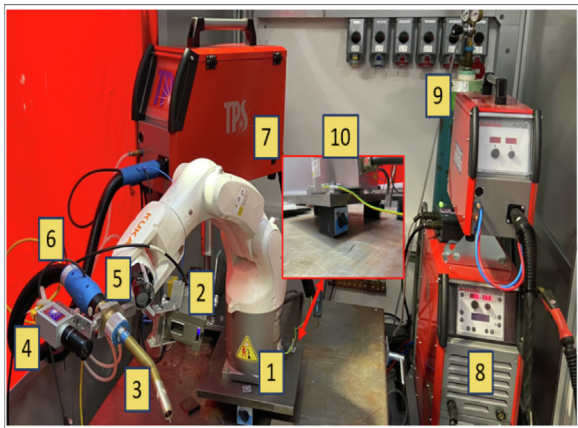


Fig. 2.8. Real-time trajectory control algorithm deployed under interpolation cycle rate of 4 ms driven from the internal clock of the robotic controller.

d_A per axis and the absolute cumulative correction D_A which adds to the initial target position P_T to avoid any possible distortion to the generated LC trajectory profile due to the summed instantaneous corrections

Benefits arising from this strategy are the generation of robotic path purely on sensor's feedback, where the TCP of the welding torch is driven in real-time and able to react to changes from the environment, while also bypassing the internal motion planning from a robotic controller, prerequisite by OP and OLP approaches. The process diagram depicted in Fig. A6 in Appendix forms part of the LC controller generating the linear d_L motion component.

3. Proof-of-Concept experimental verification

3.1. Experimental setup

A 6 DoF robotic arm with a maximum reach of 54.1 cm was transformed into a welding robot with a flexible magnetic base and a welding bracket that holds an RGB vision camera, a welding camera, a welding torch, and a laser scanner. This modularized robotic welding setup can be seen in Table 3.1.

The laser scanner (2) is used to adapt the pose of the welding torch relative to the specimen through the placement of the QR

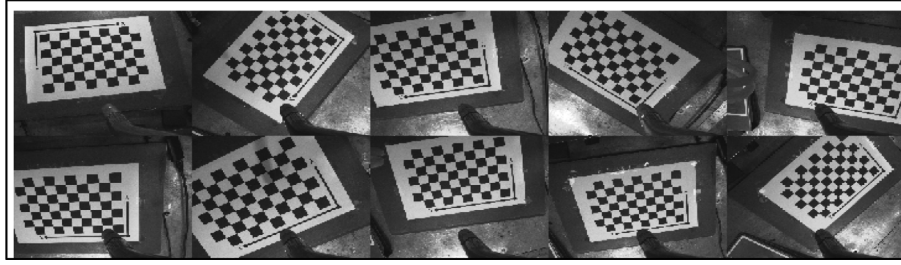


Fig. 3.1. Ten out of the thirty checkerboard poses which were used for the Hand-Eye and camera calibration.

code and extract key features and the welding reference path with a robotic speed of 5 mm/s and a positional increment of 1 mm as described in Section 2.2.2, which are used as inputs to the multi-pass welding framework [45]. The XIRIS (4) dynamic range camera is utilized to provide visual feedback of the weld pool during welding. The RGB camera (5) identifies the specimen in the scene and extracts the pose of the QR code relative to the robot motion frame through Hand-Eye calibration. The flexible magnetic base (10) allows the mounting of the robotic arm on different metallic surfaces.

For the automated welding trials, the welding process was MAG using pulsed mode to reduce the welding spatter in absolute wire-feed speed synergic mode [50–52]. A solid filler wire of 1.2 mm diameter was used along with a constant flow rate of ArCO₂ gas at 15 L/min. An embedded reconfigurable input/output cRIO 9032 controller from National Instruments [53] undertakes control of welding dynamics and robot kinematics through the developed external real-time RSI motion module. The software development took place in LabVIEW 2017 SP1 along with OpenCV 4.1 library compiled for x64 Intel real-time systems [54].

3.1.1. Camera & Hand-Eye calibration

$$\begin{bmatrix} 2.3597 & 0 & 1.1871 \\ 0 & 2.3582 & 1.0315 \\ 0 & 0 & 1 \end{bmatrix}$$

For the Hand-Eye calibration thirty different poses were captured in total (Fig. 3.1), recording at the same time the pose of the TCP relative to the robot base frame. These frames were used also for the camera calibration (intrinsic) and distortion coefficient estimation based on OpenCV [40]. Utilizing the pinhole model of the camera resulted in an intrinsics matrix.

with radial distortion coefficients $k_1 = -0.0775$, $k_2 = 0.0987$, $k_3 = -0.0093$ and a root mean square reprojection error of 0.2727 pixels. The average translation and rotational error were found to be 1.4181 mm and 0.0049 rads respectively. Finally, the TCP calibration of the welding torch using the four points method for KUKA robots, resulted in an overall error of 1.03 mm, which was acceptable since the welding torch's solid wire diameter used was 1.2 mm. The Hand Eye calibration matrix using the method developed on [38] resulted in:

$$g_{He} = \begin{bmatrix} 0.0317 & -0.0028 & 0.9995 & -236.5988 \\ 0.4691 & 0.8831 & -0.0124 & -48.9340 \\ -0.8826 & 0.4693 & 0.0293 & -18.4055 \\ . & . & 000 & 1 \end{bmatrix}$$

3.2. Adaptive extraction of features and reference welding path

The first set of experiments was undertaken to characterise the compact and automated robotic welding systems' autonomous ability to identify the location and 3D pose of single sided V-

grooves in the scene, adapting its welding torch pose relative to that, in such a way that the features of the groove can be extracted highly accurately, and the welding reference paths can be generated with high accuracy to perform welding with a forehand technique [72].

For that purpose, a V-groove joint was manually placed in four different position-orientations within a $\pm 10^\circ$ angle relative to the robot base, as can be seen in Table 3.2, acknowledging that these bounds are usually met within realistic high integrity welding configurations. The nominal geometric characteristics of the V-groove joint are recorded in Table 3.2.

In each placement, a human manually placed a square QR code of fixed edge of 60.1 mm in parallel with the main axis of welding. Choosing a 60.1 mm QR code was found to be within the depth of field of the camera which was calculated at 350 mm and the selected scene that the robotic arm operates. The robot retracts and extracts a pose of the scene and based on Section 2.1 using Eq:2:1 both translation and 3D pose of the QR code are calculated relative to the robot base. The 3D pose of the QR code represents the 3D pose of the specimen. Fig. 3.2 depicts the process of identifying the specimen's pose autonomously, utilizing the vision result of the Hand-Eye calibration, adapting the torch's pose, extracting the groove features and reference welding path for the root pass.

Following that, the geometrical features of the single sided V-groove and the welding reference path were extracted according to the algorithmic process described in Fig. 2.7. Lastly, the same process was repeated but this time the algorithms described in Section 2.2.2 were utilized where the laser sensing approach compensates for the vision and human-introduced error from the placement of the QR code. The accuracy on the extracted features of the groove was compared in both cases with the actual ones from Table 3.2, resulting in Table 3.3, where the maximum error and the percentage reduction of the error for the four different orientations with and without compensating for the vision and human error is recorded.

Table 3.4 depicts the error per pose of the welding joint on the extracted features of the groove following compensation for the vision and the human error.

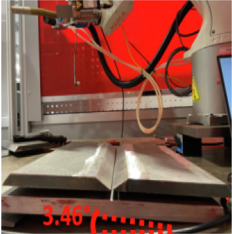
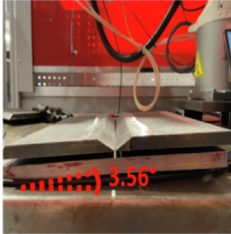

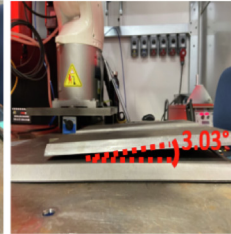
Lastly, Table 3.5 stores the maximum error on the extraction of the reference welding paths between the four different orientations when the algorithmic process described in 2.2.2 is not utilized.

Also, Fig. 3.3 depicts the error in the extracted 3D pose of the welding specimen from Table 3.2(d) which is the difference in the pose of the two depicted coordinate frames. The error on the angles was found to be $A = 0.38^\circ$, $B = 1.15^\circ$, and $C = 0.26^\circ$ after compensating with the algorithmic laser scanning process.

3.3. Automated Multi-Pass Arc welding trials

The second set of experiments was related to the deployment of fully automated welding trials for three single sided V-groove joints of structural steel grade S-275. These joints were manually

Table 3.2
Characteristics of the V-groove used for the first set of experiments.

| Four poses of the V-groove sample relative to the robot base | | | | V-Groove Characteristics | |
|---|---|---|--|--------------------------|-----|
|  |  |  |  | Groove Angle (°) | 120 |
| (a) | (b) | (c) | (d) | Root Gap (mm) | 2 |
| | | | | Root-face (mm) | 1.1 |
| | | | | Length of joint (mm) | 300 |

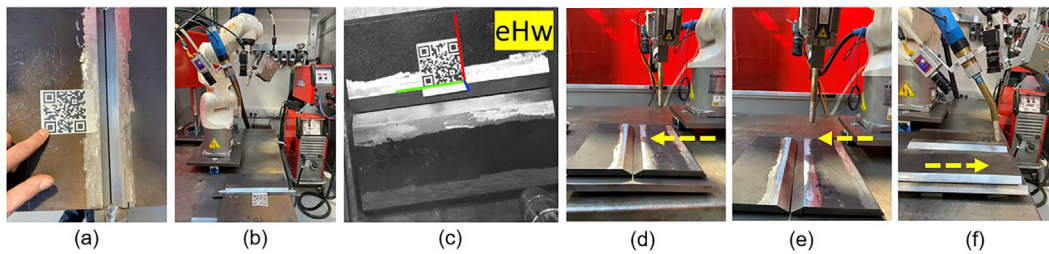


Fig. 3.2. (a) A human place the QR code in the specimen with one edge in parallel with the seam (axis of welding), (b) Robotic arm retracts to grab an image of the scene, (c) Algorithmic process described in Section 2.1 estimates the pose eHw of the QR code relative to the camera optical centre (overlayed in the image), (d) The welding system utilizes Eq:2:1 to estimate the pose of the specimen relative to the robot base in the initial position of the torch, (e) The welding torch adapts its pose relative to the specimen (Section 2.2), (f) Groove characteristics and reference welding path are extracted (see Fig. 2.7).

Table 3.3
The maximum error between the four different orientations (Table 3.2) on extracting the geometrical characteristics of the V-groove with and without compensating for the vision and human error.

| Groove Features | Error - Without Compensating | Error after Compensating (Section 2.2.2) | % Percentage error reduction after compensating |
|----------------------|------------------------------|--|---|
| Groove Angle (°) | 5.78 | 0.76 | -86.8 % |
| Root Gap (mm) | 1.03 | 0.22 | -78.6 % |
| Root-face (mm) | 1.69 | 0.11 | -93.49 % |
| Length of joint (mm) | 3 | 0.4 | -86.66 % |

placed within the robotic working volume at various $\pm 10^\circ$ angles relative to the robot base. The autonomous identification of the pose of the specimen, compensation for vision and human error and finally the utilization of the tactile and optical sensing process led to the extraction of the groove characteristics and the reference welding path. Following that the groove characteristics were used as an input to the multi-pass welding framework developed on [45] to populate the welding schedule for all welding passes per layer. The welding integrity of the developed sensor-enabled work to produce repeatable high-quality welds was verified afterwards with PAUT.

Table 3.4
Error on the extracted groove features for each pose of the joint (Table 3.2) following compensation for the vision and human introduced error.

| Groove Features | Pose (a) | Pose (b) | Pose (c) | Pose (d) | Average Error |
|----------------------|----------|----------|----------|----------|---------------|
| Groove Angle (°) | 0.00 | 0.56 | 0.28 | 0.76 | 0.40 |
| Root Gap (mm) | 0.04 | 0.07 | 0.22 | 0.10 | 0.18 |
| Root-face (mm) | 0.03 | 0.11 | 0.09 | 0.04 | 0.06 |
| Length of Joint (mm) | 0.01 | 0.09 | 0.00 | 0.40 | 0.12 |

The selected V-groove geometries used for experimental validation are commonly found in marine and manufacturing configurations where the characteristics of these were captured from the optical and tactile inspection process, recorded in Table 3.6.

The pose of each specimen from the front side relative to the robot base following the compensation for vision and human error can be seen graphically in Fig. 3.4 and is recorded in Table 3.7. The multi-pass welding framework developed on [45] was initialized with a deposition coefficient $a_H = 1.03$, weaving factor $\delta = 2mm$, total height above specimen of 1 mm and four different welding parameter combinations recorded in Table 3.8.

The cost function C(80 %,5%,15 %) was selected to achieve the minimum number of passes [45]. Fig. 3.5 depict the produced welding schedule for Joints 1 and 3 for the minimum value of the assigned cost function.

Table A6.1, Table A6.2 and Table A6.3 in the Appendix provide the produced welding schedule along with the welding parameters per layer for each welded joint respectively. Fig. 3.6 illustrates a time-lapse of 7 out of the total 14 deposited welding passes which were deposited for welding Joint 2. The whole process was automatically driven from the external real-time motion module without human intervention during welding other than cutting the wire between welding passes to avoid contamination with the subsequent passes.

Table 3.5

The maximum error in translation and rotation on the extraction of the reference welding path for both Start and End weld points between the four different orientations of the V-groove joint when the compensation for vision and human error does not take place.

| Max Path Error | X (mm) | Y (mm) | Z (mm) | A (°) | B (°) | C (°) |
|----------------|-------------|-------------|-------------|-------------|-------------|-------------|
| Start Point | 1.78 | 3.94 | 1.41 | 1.01 | 1.15 | 0.80 |
| End Point | 2.08 | 0.08 | 1.11 | 1.01 | 1.15 | 0.80 |
| In total | 2.08 | 3.94 | 1.41 | 1.01 | 1.15 | 0.80 |

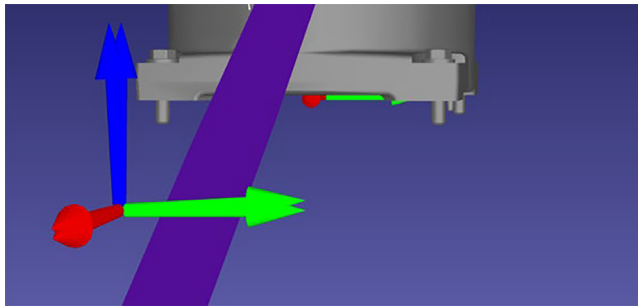


Fig. 3.3. Correcting the welding torch's pose relative to the 3D pose of the specimen, through laser scanner compensation algorithmic process (Section 2.2.2).

Table 3.6

Extracted features through the optical and tactile inspection process (Fig. 2.7) of the two single sided V-grooves following vision and human error compensation process.

| Features of V-groove | Joint 1 | Joint 2 | Joint 3 |
|-----------------------------------|---------|---------|---------|
| Thickness | 15.28 | 15.10 | 9.87 |
| Groove Angle (°) | 87.60 | 86.81 | 91.60 |
| Root Gap (mm) | 2.09 | 2.10 | 2.22 |
| Root-face (mm) | 1.80 | 1.57 | 2.06 |
| Length of joint (mm) | 299.95 | 300.02 | 299.98 |
| Root-offset (after root-pass -mm) | 3.78 | 3.35 | 3.34 |

3.3.1. Ultrasound inspection for defects

Defects on weldments arising from welding practices can affect the structural integrity and can reduce the life span of infrastructures [55]. The identification and the size of flaws on welds are examined in line with specific accepted standards and linked with their final application. Hence, the integrity of welded joints is commonly verified through NDT utilizing ultrasound inspection. PAUT as a reliable candidate for ultrasound inspection is utilized to inspect the welded samples [56,57].

The configuration for the inspection system is recorded in Table 3.9. Gain calibration was performed according to BS EN ISO 17,640 and any reflections from potential defects were compared with the reference signal. Fig. 3.7 shows the calibration process where a phased array system inspects a welded sample of 15 mm thickness with the same material composition as the manufactured weldments containing two side-drilled holes of \varnothing 2 mm. The gain was fixed at 55 dB and the signal from the side-drilled holes was received at an angle of 55° and was set to 80 % of the screen height. Adhering to the experimental calibration process each welded joint was inspected manually at room temperature along the main axis of welding.

It was decided that indications above 40 % on-screen height of the A-scans will provide a possible candidate for a defect. The PAUT inspection of the three welded joints did not give any indication for a potential defect such as lack of fusion on sidewalls or inter-pass

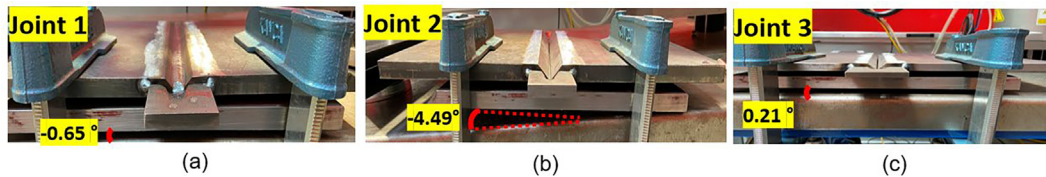


Fig. 3.4. Extracted poses following compensation of vision and human error for the three joints relative to the robot base. (a),(b),(c): Front plane angle relative to robot base, which is the angle of the specimen relative to axis Y of \$WORLD base of robot.

Table 3.7

Identified origin of QR code relative to \$WORLD base of the robot and corrected pose of the specimen following the algorithmic process from Section 2.2.2.

| Joint 1 | Identified Origin of QR code (relative to robot \$WORLD Base) | | | Orientation of QR code – Specimen (relative to robot \$WORLD Base) | | |
|----------------|---|--------|--------|--|-------|-------|
| | X (mm) | Y(mm) | Z(mm) | A (°) | B (°) | C (°) |
| Initial Pose | 370.05 | 218.8 | -21.65 | -1.24 | 2.39 | -1.78 |
| Corrected Pose | - | - | - | -1.00 | -0.65 | -0.98 |
| Joint 2 | | | | | | |
| | X (mm) | Y(mm) | Z(mm) | A (°) | B (°) | C (°) |
| Initial Pose | 383.62 | 214.32 | -15.59 | -1.49 | -0.66 | -0.45 |
| Corrected Pose | - | - | - | -0.62 | -4.49 | -0.33 |
| Joint 3 | | | | | | |
| | X (mm) | Y(mm) | Z(mm) | A (°) | B (°) | C (°) |
| Initial Pose | 374.47 | 198.32 | -29.46 | 3.01 | 2.75 | -0.91 |
| Corrected Pose | - | - | - | 2.51 | 0.21 | 0.05 |

Table 3.8
Pairs of welding parameters configuration used to generate the welding schedule for each joint.

| Welding Configuration | Robot Speed (mm/s) | Wire Feed Speed (mm/s) | Current (A) | Voltage (Volts) |
|-----------------------|--------------------|------------------------|-------------|-----------------|
| W_{c1} | 5 | 76.63 | 144 | 21.9 |
| W_{c2} | 5 | 68.3 | 131 | 21.3 |
| W_{c3} | 5.5 | 76.63 | 144 | 21.9 |
| W_{c4} | 5.5 | 68.3 | 131 | 21.3 |

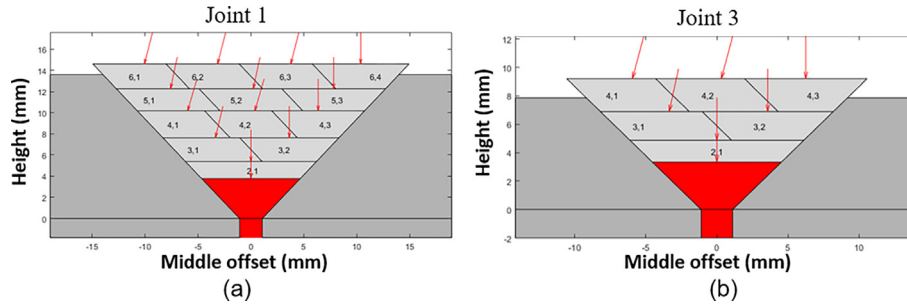


Fig. 3.5. Generated welding schedule for Joints 1 and 3 produced from the minimum value of the assigned cost function $C(80\%,5\%,15\%)$ – the red arrows represents the pose of the welding torch per welding pass [45]. (For interpretation of the references to colour in this figure legend, the reader is referred to the web version of this article.)

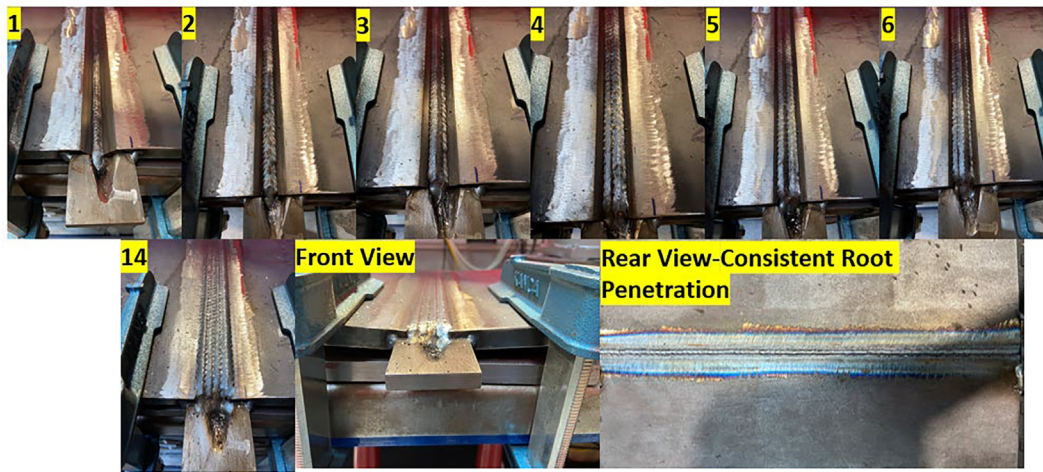


Fig. 3.6. A timelapse of 7 welding passes is depicted out of the total 14 produced from the multi-pass welding framework based on the cost function $C(80\%,5\%,15\%)$.

lack of fusion which is often encountered in thick weldments during manufacturing [4].

Fig. 3.8 depicts PAUT for Joint 1 where Fig. 4.1 collates the backside of each welding joint demonstrating repeatable and consistent root penetration.

Table 3.9
Configuration of the PAUT inspection system.

| PAUT Configuration | Value |
|---------------------------|-----------------------------|
| Probe (MHz) | 5 |
| Voltage (V) | 100 |
| Elements of the array (#) | 64 |
| Pitch (mm) | 0.5 |
| Wedge Material | Ultem |
| Wedge angle (°) | 37.6 |
| PRF (Hz) | 2000 |
| Pulse Width (ns) | 100 |
| Sector (°) | 40–75 |
| Controller | LTPA 64 T/64R(Peak NDT, UK) |

4. Discussion

Two different kinds of experiments were performed where the novelty of the proposed automated robotic developments was showcased to validate the aim of autonomous high-integrity welding with no prior CAD predefined robotic paths, or pre-defined component localisation.

The work presented herein was able to a) identify the position and the 3D pose of the as-built components to be welded in the scene and adapt its welding process to unknown and unconstrained specimens, b) extract the features of the as-built V-grooves and generate the robotic welding reference paths with no prior CAD knowledge and c) autonomously deploy all welding passes under a purely sensor-driven motion framework. PAUT inspection was undertaken to verify the lack of any defects and overall welding results, validating the proposed sensory enabled approach.

From the first set of experiments, the developed system accurately extracted the features of the single sided V-groove for all the four different poses and autonomously generated the reference

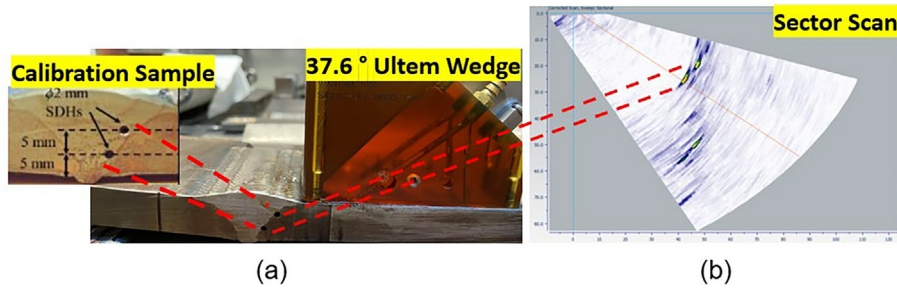


Fig. 3.7. Gain calibration at 55 dB using a welded sample with two side-drilled holes of \varnothing 2 mm for PAUT-NDT inspection.

Table A6.1
Populated welding schedule and welding parameters per layer for joint 1.

| Pass Deposited (#) | Layer Number (#) | Pass Number (#) | Wire Feed Speed (mm/s) | Robot Speed (mm/s) | Offset-middle of the seam (mm) | Height from root-face (mm) | Work Angle of torch ($^{\circ}$) | Weaving Width (mm) | Consumable Material (g) | Arc Welding Time (s) |
|--------------------|------------------|-----------------|------------------------|--------------------|--------------------------------|----------------------------|------------------------------------|--------------------|-------------------------|----------------------|
| 1 | 1 | 1 | 41.66 | 2 | 0 | 3.78 | 0 | 2.66 | 51.44 | 150 |
| 2 | 2 | 1 | 75 | 5 | 0 | 5.38 | 0 | 4.19 | 37.04 | 59.99 |
| 3 | 3 | 1 | 76.63 | 5.5 | -3.36 | 7.62 | 13.41 | 2.82 | 34.41 | 54.54 |
| 4 | 3 | 2 | 76.63 | 5.5 | 3.62 | 7.62 | 0 | 2.68 | 34.41 | 54.54 |
| 5 | 4 | 1 | 76.63 | 5.5 | -5.98 | 10.18 | 16.22 | 2.57 | 34.41 | 54.54 |
| 6 | 4 | 2 | 76.63 | 5.5 | 0.37 | 10.18 | 16.22 | 2.57 | 34.41 | 54.54 |
| 7 | 4 | 3 | 76.63 | 5.5 | 6.35 | 10.18 | 0 | 2.38 | 34.41 | 54.54 |
| 8 | 5 | 1 | 76.63 | 5.5 | -7.59 | 12.25 | 11.97 | 3.00 | 34.41 | 54.54 |
| 9 | 5 | 2 | 76.63 | 5.5 | 0.22 | 12.25 | 11.97 | 3.00 | 34.41 | 54.54 |
| 10 | 5 | 3 | 76.63 | 5.5 | 7.81 | 12.25 | 0 | 2.89 | 34.41 | 54.54 |
| 11 | 6 | 1 | 76.63 | 5.5 | -10.06 | 14.60 | 14.40 | 2.71 | 34.41 | 54.54 |
| 12 | 6 | 2 | 76.63 | 5.5 | -3.15 | 14.60 | 14.40 | 2.71 | 34.41 | 54.54 |
| 13 | 6 | 3 | 76.63 | 5.5 | 3.75 | 14.60 | 14.40 | 2.71 | 34.41 | 54.54 |
| 14 | 6 | 4 | 76.63 | 5.5 | 10.37 | 14.60 | 0 | 2.57 | 34.41 | 54.54 |

Table A6.2
Populated welding schedule and welding parameters per layer for joint 2.

| Pass Deposited (#) | Layer Number (#) | Pass Number (#) | Wire Feed Speed (mm/s) | Robot Speed (mm/s) | Offset-middle of the seam (mm) | Height from root-face (mm) | Work Angle of torch ($^{\circ}$) | Weaving Width (mm) | Consumable Material (g) | Arc Welding Time (s) |
|--------------------|------------------|-----------------|------------------------|--------------------|--------------------------------|----------------------------|------------------------------------|--------------------|-------------------------|----------------------|
| 1 | 1 | 1 | 41.66 | 2 | 0 | 3.35 | 0 | 2.23 | 51.45 | 150.01 |
| 2 | 2 | 1 | 75 | 5 | 0 | 5.08 | 0 | 3.86 | 37.05 | 60.00 |
| 3 | 3 | 1 | 76.63 | 5.5 | -3.18 | 7.41 | 14.24 | 2.73 | 35.04 | 55.54 |
| 4 | 3 | 2 | 76.63 | 5.5 | 3.48 | 7.41 | 0 | 2.58 | 35.04 | 55.54 |
| 5 | 4 | 1 | 76.63 | 5 | -5.82 | 10.26 | 17.59 | 2.70 | 37.85 | 60.00 |
| 6 | 4 | 2 | 76.63 | 5 | 0.45 | 10.26 | 17.59 | 2.70 | 37.85 | 60.00 |
| 7 | 4 | 3 | 76.63 | 5 | 6.27 | 10.26 | 0 | 2.48 | 37.85 | 60.00 |
| 8 | 5 | 1 | 76.63 | 5 | -7.63 | 12.52 | 12.71 | 3.14 | 37.85 | 60.00 |
| 9 | 5 | 2 | 76.63 | 5 | 0.25 | 12.52 | 12.71 | 3.14 | 37.85 | 60.00 |
| 10 | 5 | 3 | 76.63 | 5 | 7.88 | 12.52 | 0 | 3.01 | 37.85 | 60.00 |
| 11 | 6 | 1 | 76.63 | 5.5 | -10.20 | 14.84 | 14.15 | 2.74 | 35.04 | 55.54 |
| 12 | 6 | 2 | 76.63 | 5.5 | -3.20 | 14.84 | 14.15 | 2.74 | 35.04 | 55.54 |
| 13 | 6 | 3 | 76.63 | 5.5 | 3.79 | 14.84 | 14.15 | 2.74 | 35.04 | 55.54 |
| 14 | 6 | 4 | 76.63 | 5.5 | 10.49 | 14.84 | 0 | 2.59 | 35.04 | 55.54 |

Table A6.3
Populated welding schedule and welding parameters per layer for joint 3.

| Pass Deposited (#) | Layer Number (#) | Pass Number (#) | Wire Feed Speed (mm/s) | Robot Speed (mm/s) | Offset-middle of the seam (mm) | Height from root-face (mm) | Work Angle of torch ($^{\circ}$) | Weaving Width (mm) | Consumable Material (g) | Arc Welding Time (s) |
|--------------------|------------------|-----------------|------------------------|--------------------|--------------------------------|----------------------------|------------------------------------|--------------------|-------------------------|----------------------|
| 1 | 1 | 1 | 41.66 | 2 | 0 | 3.34 | 0 | 2.55 | 51.96 | 151.5 |
| 2 | 2 | 1 | 70 | 5 | 0 | 4.86 | 0 | 4.13 | 34.92 | 60.59 |
| 3 | 3 | 1 | 68.3 | 5.5 | -3.36 | 6.88 | 12.29 | 2.73 | 30.97 | 55.08 |
| 4 | 3 | 2 | 68.3 | 5.5 | 3.58 | 6.88 | 0 | 2.62 | 30.97 | 55.08 |
| 5 | 4 | 1 | 68.3 | 5.5 | -5.96 | 9.18 | 14.94 | 2.47 | 30.97 | 55.08 |
| 6 | 4 | 2 | 68.3 | 5.5 | 0.30 | 9.18 | 14.94 | 2.47 | 30.97 | 55.08 |
| 7 | 4 | 3 | 68.3 | 5.5 | 6.26 | 9.18 | 0 | 2.32 | 30.97 | 55.08 |

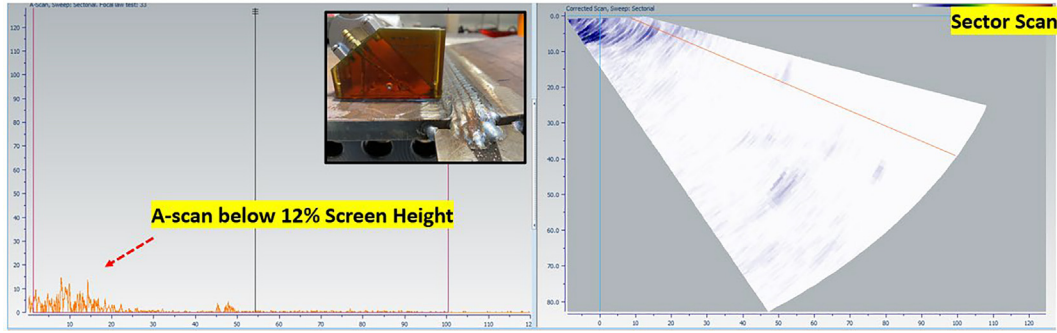


Fig. 3.8. Phased array inspection for Joint 1 along the main axis of welding resulted in indications below 12% of screen height in the A-scan.

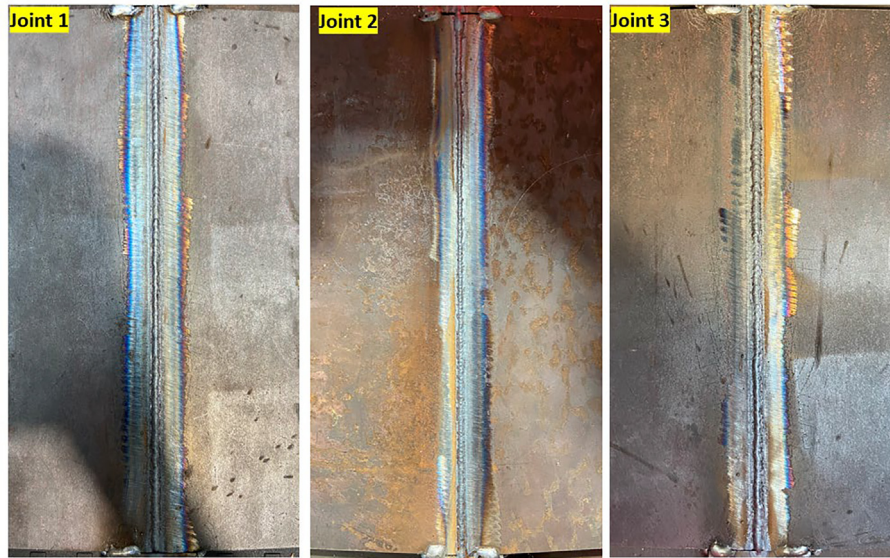


Fig. 4.1. Back-side per welded joint demonstrating consistent and repeatable root penetration.

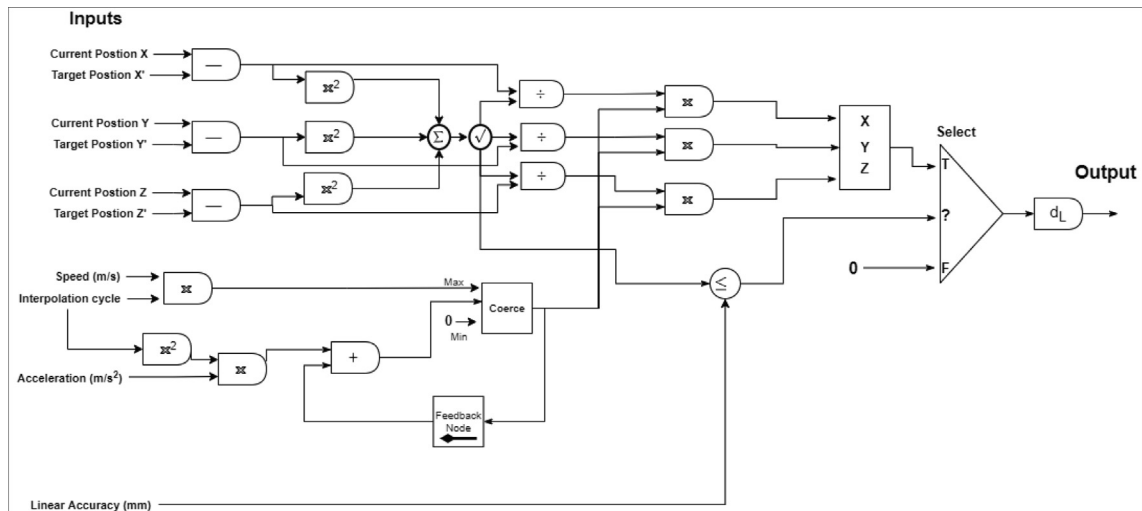


Fig. A6. 1. LC process diagram for on-the fly cartesian corrections on the X-Y-Z space based on an acceleration-cruise speed profile.

welding path. Compensating for the vision and human error from the placement of the QR code in the specimen, the algorithmically sensor-driven approach achieved a maximum error of 0.4 mm and 0.76° and on average 0.12 mm, 0.4° on the extraction of the features of the groove. This is a significant 86.38 % average reduction in the error as compared to the process which relies only on the vision outcome, where the errors reached 3 mm and 5.78°. In addition,

it was essential to adapt the pose of the welding torch relative to the welding joint, for maximum repeatable fusion, heat concentration and no defect generation. Without adaption of the pose to the specimen, a maximum error of 3.94 mm and 1.15° was observed for the reference welding path extraction, which is not acceptable for high-integrity robotic welding.

The successful automated deployment of multi-pass robotic arc welding for three V-groove joints, two of the same thickness but in different poses and for a third but thinner sample, enhance the proof of concept of the developed compact automated welding solution for repeatable high-quality welds. A maximum error of 3.04°, 3.83° and 2.54° on the identified pose of Joints 1 to 3, was corrected by the integrated algorithmic framework and the system was able to execute the full multi-pass welding schedule. The developed external real-time motion module provided the foundation for a purely sensor-driven approach, from identification, and inspection of the samples to the subsequent deployment of each welding pass.

Calibrated PAUT inspection of the welded samples validated the repeatable and defect free characteristics of the approach. The lack of common defects such as lack of root penetration, undercuts and porosity which are commonly encountered in industrial environments, reduces rework, schedule slippage and future risk in critical infrastructure.

5. Conclusion

In this paper, an autonomous sensory-driven automated welding approach based on no prior CAD knowledge, is developed, deployed, and experimentally validated. Dynamic localization of the as-built pre-welded specimen in the scene, adaption of the welding torch's pose, extraction of groove characteristics and sensor-driven generation of the reference welding paths delivers multi-specimen defect-free welds. The feasibility of the proposed work was validated by examining the structural integrity of the weldments utilizing PAUT inspection, showcasing the overall success of the automated welding approach.

To summarize, the novel work described in this paper has demonstrated:

- A reliable and consistent user-driven sequencing method for unconstrained localization of the workpiece prior to welding with the use of fiducial markers.
- An automated adaptive vision process to i) extract the geometric features of the as-built V-grooves which were placed in different poses ($\pm 10^\circ$) to align with industry relevant localisation uncertainty, ii) enable simultaneously the generation of accurate sensor-driven welding paths and iii) compensate for the vision and human error, achieving a maximum error of 0.4 mm and 0.76° on the extraction of the groove characteristics.
- An algorithmic visual-sensing approach to build the welding paths on-the-fly, eliminating the cumbersome manual teaching of pre-programmed paths based on nominal CAD.

Algorithm 1 Touch sensing routine to drive laser scanner within the groove.

ALGORITHM 1: TOUCH SENSING ROUTINE

1
2
3
4

Data: X_position, Angle_B, Times_Touched, Z_Touched_Position, Touched_Position, Z_threshold, Touching, Z_Position, Wire_Touched, Target_Z
Times_Touched \leftarrow 0; **X_position** \leftarrow 0; **Touching** \leftarrow TRUE;
Z_Position \leftarrow 0;
WHILE (Touching)
 Z_Position \leftarrow Z_position-3;
 IF Wire_Touched

- An external real-time motion module which led to full and autonomous deployment of defect-free welding on three variable placed joints relative to the robot base.

Benefits arising from the developed sensor-driven algorithmic advancements highlight the flexible and robust character of the system to deliver high-quality welding.

As a result, minimum time for setup is required between welding tasks, since there is no need to program manually robotic paths or utilize CAD designs which introduce downtime. At the same time the sensor-driven adaptive approach ensures defect free welds, validated with NDT inspection. Overall, the developed technology herein does not require any manual robot programming, nominal CAD knowledge, constrained fixturing driving down time and cost.

Future work seeks to investigate different types of weld joint geometries, such as corner, lap, and T-joints alongside mobile robot deployment via tracks. Furthermore, the presented work will be expanded to larger-scale robotics platforms with multiple DoFs based on commercial and technical requirements.

Data availability

The data that supports the findings of this study are available from the corresponding author on reasonable request.

Data availability

Data will be made available on request.

Declaration of Competing Interest

The authors declare that they have no known competing financial interests or personal relationships that could have appeared to influence the work reported in this paper.

Acknowledgements

This work was funded under the Maritime, Enterprise, Innovation and Research (MEIR) program and industrial sponsor Babcock International Group PLC.

Appendix

A1 – Demonstration of the algorithmic advances:
<https://strathcloud.sharefile.eu/d-scf2d050c3f0746a083754a3ed6a32338>

Algorithm 1 Touch sensing routine to drive laser scanner within the groove. (continued)

ALGORITHM 1: TOUCH SENSING ROUTINE

```

5           Touched_Position ← Robot_Position; Times_Touched ← Times_
           Touched + 1; Target_Z ← Z_Position + 10
6           IF Times_Touched greater than 1
7             IF abs(Angle B) greater than 5 {Z_Threshold ← 4; ELSE
           Z_Threshold ← 2;}
8             END
9             IF abs(Z_touched_Position(Times_Touched)-
           Z_Touched_Position(Times_Touched-1)) > Z_Threshold
10            Touching ← FALSE;
11            ELSE
12              X_position ← Times_Touched*(-5);
13            END
14            ELSE
15              X_position ← Times_Touched*(-5);
16            END
17            END

```

Algorithm 2 Compensates for the error in angle phi around Z axis using the start and end points from laser scanner inspection in X-Y space of frame {W}.

ALGORITHM 2: COMPENSATE FOR ERROR IN ANGLE PHI AROUND Z AXIS

```

1           Data: phi angle, x_start, x_end, y_start, y_end, actual_phi_angle, slope, theta
           slope ← (x_end-x_start)/(y_end-y_start)
2           theta ← rad2deg(atan(abs(slope)))
3           IF (slope < 0)
4             actual_phi_angle ← phi angle + theta
5           ELSE
6             actual_phi_angle ← phi angle-theta
7           END

```

Algorithm 3. Compensates for the error in angle psi around X using the start, end points from laser scanner inspection in Y-Z space of frame {W}, while keeping constant height between laser scanner emission point and specimen.

ALGORITHM 3: COMPENSATE FOR ERROR IN ANGLE PSI AROUND X AXIS

```

1           Data: psi angle, z_start, z_end, y_start, y_end, actual_psi_angle, slope, theta
           slope ← (z_end-z_start)/(y_end-y_start)
2           theta ← rad2deg(atan(abs(slope)))
3           IF (slope < 0)
4             actual_psi_angle ← psi angle + theta
5           ELSE
6             actual_psi_angle ← psi angle-theta
7           END

```

Appendix A. Supplementary material

Supplementary data to this article can be found online at <https://doi.org/10.1016/j.matdes.2022.111424>.

References

- [1] S.B. Chen, T. Qiu, T. Lin, L. Wu, J.S. Tian, W.X. Lv, Y. Zhang, Intelligent Technologies for Robotic Welding, in: T.-J. Tarn, C. Zhou, S.-B. Chen (Eds.), *Robotic Welding, Intelligence and Automation*, Springer, Berlin Heidelberg, 2004, pp. 123–143.
- [2] Y. Javadi, E. Mohseni, C.N. MacLeod, D. Lines, M. Vasilev, C. Mineo, E. Foster, S.G. Pierce, A. Gachagan, Continuous monitoring of an intentionally-manufactured crack using an automated welding and in-process inspection system, *Mater. Des.* 191 (2020), <https://doi.org/10.1016/j.matdes.2020.108655> 108655.
- [3] R. Halmshaw, *Introduction to the non-destructive testing of welded joints*, Woodhead Publishing, 1996.
- [4] N.T. Burgess, *Quality Assurance of Welded Construction*, Routledge, Hoboken, 1989. <http://public.ebookcentral.proquest.com/choice/publicfullrecord.aspx?p=242049> (accessed October 26, 2020).
- [5] M. Rajaraman, M. Dawson-Haggerty, K. Shimada, D. Bourne, Automated workpiece localization for robotic welding, in: IEEE International Conference on Automation Science and Engineering (CASE) 2013 (2013) 681–686, <https://doi.org/10.1109/CoASE.2013.6654062>.
- [6] R.W. Messler Jr, *Principles of welding: processes, physics, chemistry, and metallurgy*, John Wiley & Sons, 2008.
- [7] B. Wang, S.J. Hu, L. Sun, T. Freiheit, Intelligent welding system technologies: State-of-the-art review and perspectives, *J. Manuf. Syst.* 56 (2020) 373–391, <https://doi.org/10.1016/j.jmsys.2020.06.020>.
- [8] M.H. Ang, L. Wei, L.S. Yong, An industrial application of control of dynamic behavior of robots-a walk-through programmed welding robot, in: Proceedings 2000 ICRA. Millennium Conference. IEEE International Conference on Robotics and Automation. Symposia Proceedings (Cat. No.00CH37065), 2000: pp. 2352–2357 vol.3. 10.1109/ROBOT.2000.846378.
- [9] Z. Pan, J. Polden, N. Larkin, S.V. Duin, J. Norrish, in: *Recent Progress on Programming Methods for Industrial Robots*, in: ISR 2010, 2010, pp. 1–8.
- [10] O. Heimann, J. Guhl, Industrial Robot Programming Methods: A Scoping Review, in: IEEE International Conference on Emerging Technologies and Factory Automation (ETFA), 2020, pp. 696–703, <https://doi.org/10.1109/ETFA46521.2020.9211997>.
- [11] X. Wang, X. Zhou, Z. Xia, X. Gu, A survey of welding robot intelligent path optimization, *J. Manuf. Process.* 63 (2021) 14–23, <https://doi.org/10.1016/j.jmapro.2020.04.085>.
- [12] F. Chaumette, S. Hutchinson, *Visual servo control, Basic approaches, Part I*, 2006, p. 10.
- [13] G. Chesi, K. Hashimoto, eds., *Visual Servoing via Advanced Numerical Methods*, Springer London, London, 2010. 10.1007/978-1-84996-089-2.
- [14] A. Rout, B.B.V.L. Deepak, B.B. Biswal, Advances in weld seam tracking techniques for robotic welding: A review, *Rob. Comput. Integr. Manuf.* 56 (2019) 12–37, <https://doi.org/10.1016/j.rcim.2018.08.003>.
- [15] A. Zych, Programming of Welding Robots in Shipbuilding, *Procedia CIRP.* 99 (2021) 478–483, <https://doi.org/10.1016/j.procir.2021.03.107>.
- [16] K.T. Gunnarsson, F.B. Prinz, CAD Model-Based Localization of Parts in Manufacturing, *Computer* 20 (1987) 66–74, <https://doi.org/10.1109/MC.1987.1663663>.
- [17] Z.H. Xiong, Y.X. Chu, G.F. Liu, Z.X. Li, Workpiece localization and computer aided setup system, in: Proceedings 2001 IEEE/RSJ International Conference on Intelligent Robots and Systems. Expanding the Societal Role of Robotics in the the Next Millennium (Cat. No.01CH37180), 2001: pp. 1141–1146 vol.2. 10.1109/IROS.2001.976322.
- [18] S. Chen, J. Liu, B. Chen, X. Suo, Universal fillet weld joint recognition and positioning for robot welding using structured light, *Rob. Comput. Integr. Manuf.* 74 (2022), <https://doi.org/10.1016/j.rcim.2021.102279> 102279.
- [19] G. Schleth, A. Kuss, W. Kraus, Workpiece localization methods for robotic welding - a review, in: ISR 2018; 50th International Symposium on Robotics, 2018: pp. 1–6.
- [20] Final Report Summary - MARWIN (Decision making and augmented reality support for automatic welding installations) | Report Summary | MARWIN | FP7-SME | CORDIS | European Commission, (n.d.). <https://cordis.europa.eu/project/rcn/101118/reporting/en> (accessed February 15, 2019).
- [21] (n.d.) (2021), accessed January 25 <https://cordis.europa.eu/project/id/5369>.
- [22] E.B. Njaastad, O. Egeland, Automatic Touch-Up of Welding Paths Using 3D Vision, *IFAC-PapersOnLine.* 49 (2016) 73–78, <https://doi.org/10.1016/j.ifacol.2016.12.164>.
- [23] A. Kuss, U. Schneider, T. Dietz, A. Verl, Detection of Assembly Variations for Automatic Program Adaptation in Robotic Welding Systems, in: In: Proceedings of ISR 2016: 47st International Symposium on Robotics, 2016, pp. 1–6.
- [24] C.-H. Wu, S.-Y. Jiang, K.-T. Song, CAD-based pose estimation for random bin-picking of multiple objects using a RGB-D camera, in: In: 2015 15th International Conference on Control, Automation and Systems (ICCAS), 2015, pp. 1645–1649, <https://doi.org/10.1109/ICCAS.2015.7364621>.
- [25] Ø. Skotheim, M. Lind, P. Ystgaard, S.A. Fjerdings, A flexible 3D object localization system for industrial part handling, in: IEEE/RSJ International Conference on Intelligent Robots and Systems 2012 (2012) 3326–3333, <https://doi.org/10.1109/IROS.2012.6385508>.
- [26] F. Spennath, M. Palzkill, A. Pott, A. Verl, Object recognition: Bin-picking for industrial use, in: IEEE ISR 2013 (2013) 1–3, <https://doi.org/10.1109/ISR.2013.6695743>.
- [27] J.J. Rodrigues, J.-S. Kim, M. Furukawa, J. Xavier, P. Aguiar, T. Kanade, 6D pose estimation of textureless shiny objects using random ferns for bin-picking, in: IEEE/RSJ International Conference on Intelligent Robots and Systems 2012 (2012) 3334–3341, <https://doi.org/10.1109/IROS.2012.6385680>.
- [28] M. Dinham, G. Fang, Autonomous weld seam identification and localisation using eye-in-hand stereo vision for robotic arc welding, *Rob. Comput. Integr. Manuf.* 29 (2013) 288–301, <https://doi.org/10.1016/j.rcim.2013.01.004>.
- [29] L. Yang, E. Li, T. Long, J. Fan, Z. Liang, A Novel 3-D Path Extraction Method for Arc Welding Robot Based on Stereo Structured Light Sensor, *IEEE Sens. J.* 19 (2019) 763–773, <https://doi.org/10.1109/JSEN.2018.2877976>.
- [30] M. Dinham, G. Fang, in: A Low Cost HAnd-eye CALibration Method for Arc Welding Robots, IEEE, Guilin, China, 2009, pp. 1889–1893, <https://doi.org/10.1109/ROBIO.2009.5420552>.
- [31] M. Dinham, G. Fang, Weld seam detection using computer vision for robotic Arc Welding, in: IEEE International Conference on Automation Science and Engineering (CASE) 2012 (2012) 771–776, <https://doi.org/10.1109/CoASE.2012.6386339>.
- [32] M. Kong, F. Shi, S. Chen, T. Lin, Recognition of the initial position of weld based on the corner detection for welding robot in global environment, *Robotic Welding, Intelligence and Automation*, Springer (2007) 249–255.
- [33] K. Micallef, G. Fang, M. Dinham, Automatic Seam Detection and Path Planning in Robotic Welding, in: T.-J. Tarn, S.-B. Chen, G. Fang (Eds.), *Robotic Welding, Intelligence and Automation*, Springer, Berlin Heidelberg, 2011, pp. 23–32.
- [34] M. Dinham, G. Fang, J.J. Zou, Experiments on Automatic Seam Detection for a MIG Welding Robot, in: H. Deng, D. Miao, J. Lei, F.L. Wang (Eds.), *Artificial Intelligence and Computational Intelligence*, Springer, Berlin Heidelberg, 2011, pp. 390–397.
- [35] A. Ryberg, M. Ericsson, A.-K. Christiansson, K. Eriksson, J. Nilsson, M. Larsson, Stereo vision for path correction in off-line programmed robot welding, in: IEEE International Conference on Industrial Technology 2010 (2010) 1700–1705, <https://doi.org/10.1109/ICIT.2010.5472442>.
- [36] L. Shao, J. Han, D. Xu, J. Shotton, Computer vision for RGB-D sensors: Kinect and its applications [special issue intro.], *IEEE Transactions on Cybernetics.* 43 (2013) 1314–1317, <https://doi.org/10.1109/TCYB.2013.2276144>.
- [37] M.B. Shaikh, D. Chai, RGB-D Data-Based Action Recognition: A Review, *Sensors* 21 (2021) 4246, <https://doi.org/10.3390/s21124246>.
- [38] R.Y. Tsai, R.K. Lenz, A new technique for fully autonomous and efficient 3D robotics hand/eye calibration, *IEEE Trans Rob Autom* 5 (1989) 345–358, <https://doi.org/10.1109/70.34770>.
- [39] R. Tsai, A versatile camera calibration technique for high-accuracy 3D machine vision metrology using off-the-shelf TV cameras and lenses, *IEEE Journal on Robotics and Automation.* 3 (1987) 323–344, <https://doi.org/10.1109/JRA.1987.1087109>.
- [40] Z. Zhang, A flexible new technique for camera calibration, *IEEE Trans. Pattern Anal. Mach. Intell.* 22 (2000) 1330–1334, <https://doi.org/10.1109/34.888718>.
- [41] F. Vanegas, F. Gonzalez, Enabling UAV Navigation with Sensor and Environmental Uncertainty in Cluttered and GPS-Denied Environments, *Sensors* 16 (2016) 666, <https://doi.org/10.3390/s16050666>.
- [42] G. Zhenglong, F. Qiang, Q. Quan, Pose Estimation for Multicopters Based on Monocular Vision and AprilTag, in: 2018 37th Chinese Control Conference (CCC), 2018: pp. 4717–4722. 10.23919/ChiCC.2018.8483685.
- [43] X.-S. Gao, X.-R. Hou, J. Tang, H.-F. Cheng, Complete solution classification for the perspective-three-point problem, *IEEE Trans. Pattern Anal. Mach. Intell.* 25 (2003) 930–943, <https://doi.org/10.1109/TPAMI.2003.1217599>.
- [44] R. O'Brien, *Welding handbook*, vol. 2, American Welding Society. (1991).
- [45] C. Loukas, V. Williams, R. Jones, M. Vasilev, C.N. MacLeod, G. Dobie, J. Sibson, S. G. Pierce, A. Gachagan, A cost-function driven adaptive welding framework for multi-pass robotic welding, *J. Manuf. Process.* 67 (2021) 545–561, <https://doi.org/10.1016/j.jmapro.2021.05.004>.
- [46] Sensors & Measurement Systems | Micro-Epsilon, (n.d.). <https://www.micro-epsilon.co.uk/> (accessed June 27, 2019).
- [47] H.P. Vinutha, B. Poornima, B.M. Sagar, Detection of Outliers Using Interquartile Range Technique from Intrusion Dataset, in: S.C. Satapathy, J.M.R.S. Tavares, V. Bhateja, J.R. Mohanty (Eds.), *Information and Decision Systems*, Springer, Singapore, 2018, pp. 511–518, https://doi.org/10.1007/978-981-10-7563-6_53.
- [48] KUKA R.S.I. 4.0, (n.d.). <https://xpert.kuka.com/ID/AR16559> (accessed November 12, 2020).
- [49] M. Vasilev, C.N. MacLeod, C. Loukas, Y. Javadi, R.K.W. Vithanage, D. Lines, E. Mohseni, S.G. Pierce, A. Gachagan, Sensor-Enabled Multi-Robot System for Automated Welding and In-Process Ultrasonic NDE, *Sensors* 21 (2021) 5077, <https://doi.org/10.3390/s21155077>.
- [50] T. Era, T. Ueyama, Spatter reduction in GMAW by current waveform control, *Weld. Int.* 21 (2007) 496–501, <https://doi.org/10.1080/09507110701579647>.
- [51] S.H. Lee, J.S. Kim, B.Y. Lee, S.Y. Lee, The effect of external electromagnetic force in gas metal arc welding on the transfer mode, *Key Eng. Mater.* 297–300 (2005) 2825–2830, <https://doi.org/10.4028/www.scientific.net/KEM.297-300.2825>.

- [52] Z. Wang, D. Jiang, J. Wu, M. Xu, A review on high-frequency pulsed arc welding, *J. Manuf. Process.* 60 (2020) 503–519, <https://doi.org/10.1016/j.jmapro.2020.10.054>.
- [53] NI cRIO-9032 User Manual - National Instruments, (n.d.) 42.
- [54] G. Bradski, *The OpenCV Library*, Dr. Dobb's J. Software Tools. (2000).
- [55] W. Fricke, Fatigue analysis of welded joints: state of development, *Mar. Struct.* 16 (2003) 185–200.
- [56] A. Erhard, G. Schenk, T.h. Hauser, U. Völz, New applications using phased array techniques, *Nucl. Eng. Des.* 206 (2001) 325–336, [https://doi.org/10.1016/S0029-5493\(00\)00419-2](https://doi.org/10.1016/S0029-5493(00)00419-2).
- [57] E. Mohseni, Y. Javadi, N.E. Sweeney, D. Lines, C.N. MacLeod, R.K.W. Vithanage, Z. Qiu, M. Vasilev, C. Mineo, P. Lukacs, E. Foster, S.G. Pierce, A. Gachagan, Model-assisted ultrasonic calibration using intentionally embedded defects for in-process weld inspection, *Mater. Des.* 198 (2021), <https://doi.org/10.1016/j.matdes.2020.109330> 109330.